RESEARCH ARTICLE | JULY 14 2021

Electrical characterization of AlGaN/GaN heterostructures under Ohmic metals by using multi-probe Hall devices

Kazuya Uryu; Shota Kiuchi; Toshi-kazu Suzuki

Appl. Phys. Lett. 119, 023505 (2021)
https://doi.org/10.1063/5.0054553

Applied Physics Letters ARTICLE scitation.org/journal/apl

Electrical characterization of AlGaN/GaN heterostructures under Ohmic metals by using multi-probe Hall devices

Cite as: Appl. Phys. Lett. **119**, 023505 (2021); doi: 10.1063/5.0054553
Submitted: 19 April 2021 · Accepted: 28 June 2021 ·
Published Online: 14 July 2021

View Online Export Citation CrossMark

Kazuya Uryu,[1,2] Shota Kiuchi,[1] and Toshi-kazu Suzuki[1,a)]

AFFILIATIONS

[1]Center for Nano Materials and Technology, Japan Advanced Institute of Science and Technology (JAIST), 1-1 Asahidai, Nomi, Ishikawa 923-1292, Japan
[2]Advantest Laboratories Ltd., 48-2 Matsubara, Kami-Ayashi, Aoba-ku, Sendai, Miyagi 989-3124, Japan

[a)]Author to whom correspondence should be addressed: tosikazu@jaist.ac.jp

ABSTRACT

By using multi-probe Hall devices, we characterized electrical properties of AlGaN/GaN heterostructures under Ohmic metals. The characterization makes it possible to evaluate the sheet resistance, the sheet electron concentration, and the electron mobility of AlGaN/GaN heterostructures after Ohmic contact formation, by analyzing the voltage and current distribution based on a transmission line model. As a result, we find a decrease in the sheet resistance under an Ohmic metal with a decrease in the specific Ohmic contact resistivity, attributed to significant increase in the sheet electron concentration. The high sheet electron concentration indicates a parallel conduction in the AlGaN and GaN layers, caused by a high doping concentration of the near-surface AlGaN $\gtrsim 2 \times 10^{19}\,\mathrm{cm}^{-3}$, which leads to an Ohmic contact dominated by field-emission. Moreover, it is suggested that polarization doping induced by a strain in the AlGaN layer has a contribution to the high doping concentration. Multi-probe Hall devices provide a useful method to characterize electrical properties of semiconductors under Ohmic metals.

For all kinds of semiconductor devices, formation of Ohmic contacts is a key technological element. In general, electrical properties of semiconductors are modified by formation of Ohmic contacts; the sheet resistance ρ_{sk}, the sheet electron concentration n_s, and the electron mobility μ_s under the formed Ohmic metal are different from those before the Ohmic contact formation, ρ_{sh}, n_{s0}, and μ_{s0}. Electrical characterization of the semiconductor under the formed Ohmic metal is not straightforward, because a measurement current is distributed both in the semiconductor and the Ohmic metal. In order to evaluate the sheet resistance ρ_{sk}, the end contact resistance method has been developed and employed for Si-based,[1] GaAs-based,[2–5] GaN-based,[6–9] and graphene-based[10,11] devices. Moreover, the floating contact resistance method, which is theoretically equivalent to the end contact resistance method, has also been employed for GaAs-based[12] and InP-based[13,14] devices. However, these methods cannot measure the sheet electron concentration n_s and the electron mobility μ_s, which are very important information of the electrical properties of semiconductors under Ohmic metals.

There have been many attempts to obtain good Ohmic contacts to wide-gap GaN-based materials.[15] For AlGaN/GaN heterostructures, many kinds of Ohmic metal structures, such as Ti/Al-based[16–18] or Ta/Al-based[19,20] multilayers, have been investigated, where an Ohmic contact through the AlGaN energy barrier is formed by an electrical coupling between the surface Ohmic metal and the underlying two dimensional electron gas (2DEG) channel in the AlGaN/GaN heterostructure, usually achieved by the annealing process after the surface metal deposition. In order to elucidate how the coupling occurs, it is important to characterize the electrical properties of the AlGaN/GaN heterostructures under Ohmic metals. While it was suggested that the electrical properties are modified by the annealing process,[21–24] the end contact resistance method clearly showed that the sheet resistance ρ_{sk} of AlGaN/GaN heterostructures after Ohmic contact formation decreases in comparison with ρ_{sh} before Ohmic contact formation.[6–9] On the other hand, as pointed above, the sheet electron concentration n_s and the electron mobility μ_s of AlGaN/GaN heterostructures under Ohmic metals have not been measured.

In this work, for AlGaN/GaN heterostructures under Ohmic metals, in order to evaluate the sheet electron concentration n_s and the electron mobility μ_s, as well as the sheet resistance ρ_{sk}, we fabricated multi-probe Hall devices for electrical characterization. By analyzing

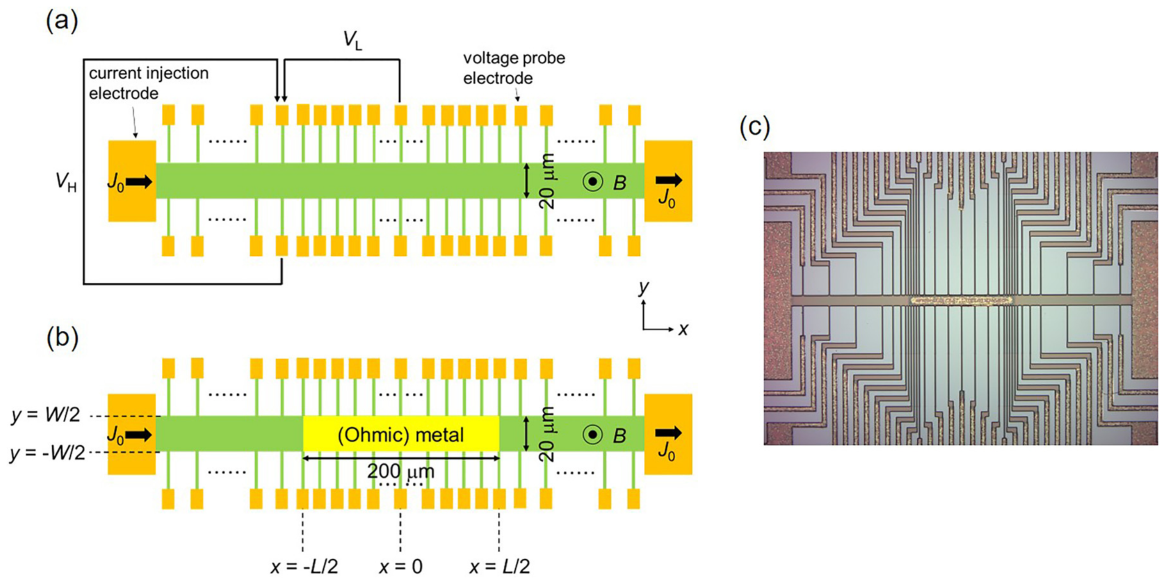

FIG. 1. The schematic top view of multi-probe Hall devices: (a) sample A and (b) samples B–D. (c) The optical image of the resist pattern for device isolation.

the voltage and current distribution based on a transmission line model, we find that, a decrease in ρ_{sk} under an Ohmic metal with a decrease in the specific Ohmic contact resistivity is attributed to a significant increase in n_s. We also employed the floating contact resistance method, which has not been applied to GaN-based devices previously. Concerning the sheet resistance ρ_{sk} and the specific contact resistivity ρ_c, the results of the multi-probe Hall devices are consistent with the floating contact resistances. It should be noted that the floating contact resistance method cannot characterize the sheet electron concentration n_s and the electron mobility μ_s, which can be evaluated by the multi-probe Hall devices. The high sheet electron concentration n_s indicates a parallel conduction in the AlGaN and GaN layers, caused by a high doping concentration of the near-surface AlGaN $\gtrsim 2 \times 10^{19}\,\mathrm{cm}^{-3}$, which leads to an Ohmic contact dominated by field-emission. The obtained results suggest that polarization doping induced by a strain in the AlGaN layer has a contribution to the high doping concentration.

Using an undoped-$Al_{0.24}Ga_{0.76}N$ (20 nm)/GaN (3000 nm) heterostructure, where no AlN spacer is employed, with $\rho_{sh} \sim 530\ \Omega/\square$, $n_{s0} \sim 8 \times 10^{12}\,\mathrm{cm}^{-2}$, and $\mu_{s0} \sim 1500\,\mathrm{cm}^2/\mathrm{V\text{-}s}$, grown by metal-organic chemical vapor deposition on sapphire (0001), we fabricated four types of multi-probe Hall devices, shown in Figs. 1(a) (sample A) and 1(b) (samples B, C, and D). Using a resist pattern shown in Fig. 1(c), the channel regions with a width of $W = 20\,\mu$m were defined by ion implantation-based device isolation. According to the x–y coordinates shown in Fig. 1 with the origin at the center of the channel, the channel region is $-320 \le x \le +320\,\mu$m and $-10 \le y \le +10\,\mu$m. The devices have a pair of current injection electrodes, and 31 pairs of voltage probe electrodes with an arm width of $2\,\mu$m. The more number of voltage probe electrodes there are, the more accurate voltage distribution can be measured. The employed number of the voltage probe electrodes is sufficient to measure the voltage distribution precisely as shown later. While the channel is not covered by a metal for sample A (w/o metal) as shown in Fig. 1(a), for samples B, C, and D, as shown in Fig. 1(b), Ti/Al/Ti/Au metals with a length of $L = 200\,\mu$m and a width of $W = 20\,\mu$m were formed on the channels; the metal region is $-100 \le x \le +100\,\mu$m and $-10 \le y \le +10\,\mu$m. For sample B, annealing was not carried out, and thus no Ohmic contact is formed between the Ti/Al/Ti/Au metal and the AlGaN/GaN semiconductor (no Ohmic). On the other hand, the Ohmic contact resistance R_c is $\sim 3\,\Omega\,$mm for sample C (higher Ohmic) and $\lesssim 1\,\Omega\,$mm for sample D (lower Ohmic), obtained by different low-temperature annealing processes at $<600\,^\circ$C. Simultaneously, we fabricated floating contact resistors[14] on the same chip for samples B, C, and D. Applying measurement current densities $-15 \le J_0 \le +15\,\mathrm{mA/mm}$ through the current injection electrodes, we measured the voltage drops by using the voltage probe electrodes; as defined in Fig. 1, we obtained $V_L(x)$ for no magnetic field $B = 0$ and $V_H(x)$ for a magnetic field $B = 0.32$ T as a function of the position x.

In order to analyze the measured voltages $V_L(x)$ and $V_H(x)$ of the multi-probe Hall devices, the AlGaN/GaN semiconductor with the Ohmic metal $(-L/2 \le x \le +L/2$ and $-W/2 \le y \le +W/2)$ is described by a transmission line model shown in Fig. 2, which gives

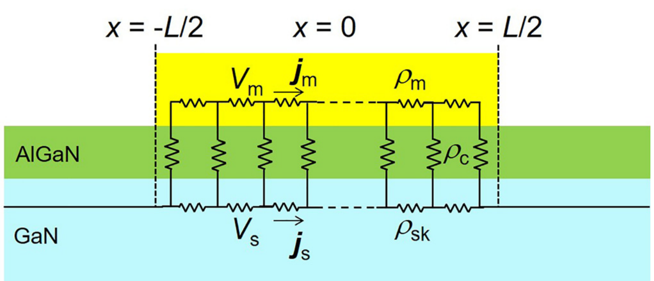

FIG. 2. A transmission line model of the AlGaN/GaN semiconductor with the Ohmic metal.

$$\boldsymbol{j}_{\rm s} = -\frac{1}{(1+\mu_{\rm s}^2B^2)\rho_{\rm sk}}\begin{pmatrix}1 & -\mu_{\rm s}B\\ \mu_{\rm s}B & 1\end{pmatrix}{\rm grad}\,V_{\rm s}$$
$$= -\frac{1}{\widetilde{\rho_{\rm sk}}}\begin{pmatrix}1 & -\mu_{\rm s}B\\ \mu_{\rm s}B & 1\end{pmatrix}{\rm grad}\,V_{\rm s}, \tag{1}$$

$$\boldsymbol{j}_{\rm m} = -\frac{1}{(1+\mu_{\rm m}^2B^2)\rho_{\rm m}}\begin{pmatrix}1 & -\mu_{\rm m}B\\ \mu_{\rm m}B & 1\end{pmatrix}{\rm grad}\,V_{\rm m}$$
$$= -\frac{1}{\widetilde{\rho_{\rm m}}}\begin{pmatrix}1 & -\mu_{\rm m}B\\ \mu_{\rm m}B & 1\end{pmatrix}{\rm grad}\,V_{\rm m}, \tag{2}$$

$${\rm div}\,\boldsymbol{j}_{\rm s} = -\frac{V_{\rm s}-V_{\rm m}}{\rho_{\rm c}} \quad\text{and}\quad {\rm div}\,\boldsymbol{j}_{\rm m} = -\frac{V_{\rm m}-V_{\rm s}}{\rho_{\rm c}}, \tag{3}$$

where $V_{\rm s}(x,y)$ and $V_{\rm m}(x,y)$ are the electrical potentials, $\boldsymbol{j}_{\rm s}$ and $\boldsymbol{j}_{\rm m}$ are the current densities [in the unit of (A/mm)], $\rho_{\rm sk}$ and $\rho_{\rm m}$ are the sheet resistances, $\mu_{\rm s}$ and $\mu_{\rm m}$ are the electron mobilities, in the semiconductor and the metal, respectively, and $\rho_{\rm c}$ is the specific contact resistivity between the semiconductor and the metal. For $B=0$, Eqs. (1)–(3) can be solved by the boundary conditions of $\mathrm{d}V_{\rm s}/\mathrm{d}x|_{x=\pm L/2} = -\rho_{\rm sk}J_0$ and $\mathrm{d}V_{\rm m}/\mathrm{d}x|_{x=\pm L/2} = 0$, leading to

$$V_{\rm L}(x) = V_{\rm s}(x,\pm W) = -\frac{\rho_{\rm sk}J_0}{\rho_{\rm sk}+\rho_{\rm m}}\left(\rho_{\rm m}x + \rho_{\rm sk}\frac{\sinh(\gamma_0 x)}{\gamma_0\cosh(\gamma_0 L/2)}\right) \tag{4}$$

and

$$j_{\rm s}(x) = \frac{J_0}{\rho_{\rm sk}+\rho_{\rm m}}\left(\rho_{\rm m} + \rho_{\rm sk}\frac{\cosh(\gamma_0 x)}{\cosh(\gamma_0 L/2)}\right), \tag{5}$$

where $\gamma_0 = \sqrt{(\rho_{\rm sk}+\rho_{\rm m})/\rho_{\rm c}}$.[14] On the other hand, for $B \neq 0$, we obtain

$$V_H(x) = V_{\rm s}(x,+W/2) - V_{\rm s}(x,-W/2),$$
$$= \frac{\mu_{\rm s}BWJ_0\widetilde{\rho_{\rm sk}}}{\widetilde{\rho_{\rm sk}}+\widetilde{\rho_{\rm m}}}\left(\widetilde{\rho_{\rm m}} + \widetilde{\rho_{\rm sk}}\frac{\cosh(\gamma_0 x)}{\cosh(\gamma_0 L/2)}\right)$$
$$+\ \text{higher-order terms}, \tag{6}$$

where the higher-order terms are given by hyperbolic functions $\cosh(k_n x)$ and $\cosh(\kappa_n x)$ with $k_n = n\pi/W$, $\kappa_n = \sqrt{\gamma_B^2 + k_n^2}$ $(n = 1, 3, \ldots)$, and $\gamma_B = \sqrt{(\widetilde{\rho_{\rm sk}}+\widetilde{\rho_{\rm m}})/\rho_{\rm c}}$.[25] Since the hyperbolic function terms are negligible at $x=0$ for sufficiently large L, we find

$$\frac{V_{\rm H}(0)}{j_{\rm s}(0)BW} \simeq \mu_{\rm s}\rho_{\rm sk} = \frac{1}{qn_{\rm s}}, \tag{7}$$

where q is the electron charge. This shows that we can measure the sheet electron concentration $n_{\rm s}$ and the electron mobility $\mu_{\rm s}$ of the AlGaN/GaN semiconductor under the Ohmic metal.

Figure 3 shows the measured $V_{\rm L}(x)/J_0$ of the multi-probe Hall devices. As shown in the inset of Fig. 3, the linear behavior for samples A and B is observed because of no Ohmic contact, giving $\rho_{\rm sh} \simeq 530\,\Omega/\Box$ for sample A and $\rho_{\rm sk} \simeq 540\,\Omega/\Box$ for sample B. This indicates that the sheet resistance is almost unchanged by the metal deposition without annealing. For samples C and D, as shown in Fig. 3, we can obtain good fitting using (4), which gives $\rho_{\rm sk} = (400 \pm 20)\,\Omega/\Box$ and $\rho_{\rm c} = (1.7 \pm 0.1) \times 10^{-4}\,\Omega\,{\rm cm}^2$ for sample C, $\rho_{\rm sk} = (330 \pm 40)\,\Omega/\Box$ and $\rho_{\rm c} = (2.6 \pm 0.4) \times 10^{-5}\,\Omega\,{\rm cm}^2$ for sample D, and $\rho_{\rm m} \sim 2\,\Omega/\Box$.

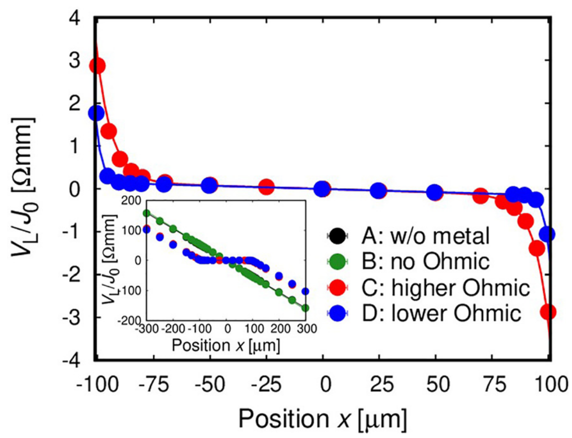

FIG. 3. The measured $V_{\rm L}/J_0$ for samples C and D as a function of the position $-100 \leq x \leq +100\,\mu m$ with the fitting curves. The inset: the measured $V_{\rm L}/J_0$ for samples A–D as a function of the position $-300 \leq x \leq +300\,\mu m$.

We find that $\rho_{\rm sk}$ decreases with a decrease in $\rho_{\rm c}$. We also carried out measurements of the floating contact resistance $R_{\rm fc}$, which is defined in the inset of Fig. 4, and given by

$$R_{\rm fc} = \frac{\rho_{\rm sk}L_{\rm fc}}{\rho_{\rm sk}+\rho_{\rm m}}\left(\rho_{\rm m} + \rho_{\rm sk}\frac{\tanh(\gamma_0 L_{\rm fc}/2)}{\gamma_0 L_{\rm fc}/2}\right) \tag{8}$$

as a function of the floating contact length $L_{\rm fc}$.[14] Figure 4 shows the measured $R_{\rm fc}$ as a function of $L_{\rm fc}$ with the curves using the results obtained by the multi-probe Hall devices. While sample B of course shows linear behavior (the inset), samples C and D show nonlinear one in good agreement with the curves; the multi-probe Hall measurement results are consistent with the floating contact resistances.

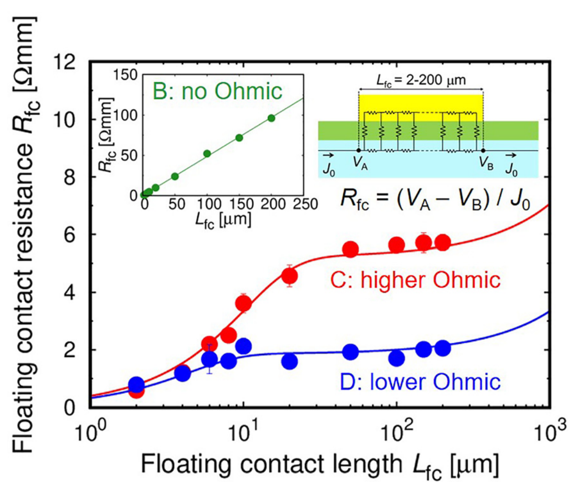

FIG. 4. The measured floating contact resistance $R_{\rm fc}$ for samples C and D as a function of the floating contact length $L_{\rm fc}$ with the curves using the results obtained by the multi-probe Hall devices. The left inset: $R_{\rm fc}$ for sample B as a function of $L_{\rm fc}$. The right inset: the configuration of the floating contact resistors.

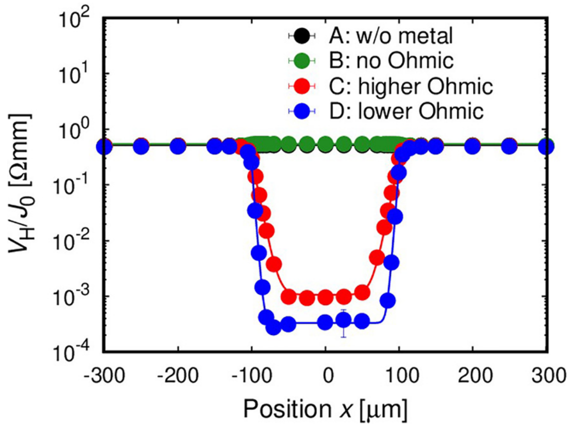

FIG. 5. The measured V_H for $B = 0.32$ T as a function of the position x with the fitting curves.

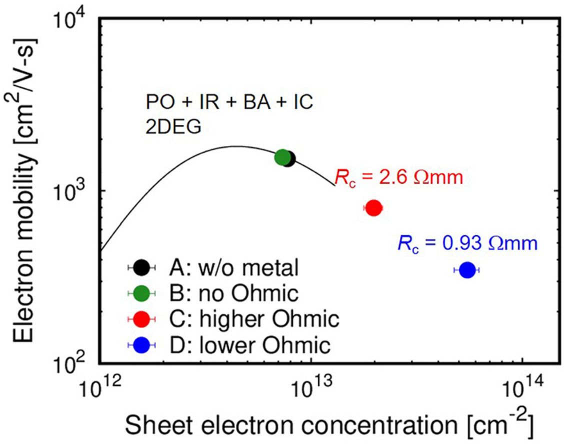

FIG. 6. The relation between the measured sheet electron concentration and the electron mobility. The curve shows the theoretical relation for the 2DEG channel (up to the maximum sheet electron concentration without a parallel conduction $\sim 1.3 \times 10^{13}$ cm^{-2}), considering polar optical phonon, interface roughness, barrier alloy, and interface charge scatterings.

Figure 5 shows the measured $V_H(x)/J_0$ for $B = 0.32$ T. We of course observe constant behavior for samples A and B due to no Ohmic contact, giving n_{s0} and μ_{s0} for sample A and n_s and μ_s for sample B. For samples C and D, we can obtain good fitting using (6), and n_s and μ_s determined by (7). The obtained properties are summarized in Table I. While n_s and μ_s for sample B are unchanged from n_{s0} and μ_{s0}, we find that, with a decrease in ρ_c, n_s significantly increases; the decrease in ρ_{sk} is due to the increase in n_s. In particular, sample D, lower Ohmic, exhibits a high sheet electron concentration of $\sim 5.5 \times 10^{13}$ cm^{-2}, suggesting that high doping takes place in the semiconductor under the Ohmic metal.

Figure 6 shows the relation between the measured sheet electron concentration and the electron mobility, n_s and μ_s, and also n_{s0} and μ_{s0}. The curve in Fig. 6 shows the theoretical relation of the sheet electron concentration and the electron mobility in the 2DEG channel, where polar optical phonon (PO),[26] interface roughness (IR),[27–29] barrier alloy (BA),[30] and interface charge (IC)[29] scatterings are taking into account to reproduce the results for samples A and B. Above the mid 10^{12} cm^{-2} of n_s, the dominant scattering mechanisms are PO (leading to a mobility $\sim n_s^{-1/3}$), IR ($\sim n_s^{-2}$), and BA ($\sim n_s^{-2}$), which, respectively, give $\sim$2000, $\sim$6000, and $\sim$15 000 cm^2/V-s for $n_s \sim 1 \times 10^{13}$ cm^{-2}. The theoretical curve is shown up to the sheet electron concentration of $\sim 1.3 \times 10^{13}$ cm^{-2}, which is the maximum value in the 2DEG channel without a parallel conduction in the AlGaN layer. For samples C and D, $n_s > 1.3 \times 10^{13}$ cm^{-2} indicates that a parallel conduction takes place in the AlGaN layer; it is suggested that the AlGaN layer has electrons of $\sim 7 \times 10^{12}$ cm^{-2} for sample C and $\sim 4 \times 10^{13}$ cm^{-2} for sample D, and thus a doping concentration N_D of the 20 nm thickness AlGaN layer is $> 3.5 \times 10^{18}$ cm^{-3} for sample C and $> 2 \times 10^{19}$ cm^{-3} for sample D.

The estimation of N_D suggests that, around room temperature $T \sim 300$ K, the conduction between the Ohmic metal and the semiconductor is dominated by thermionic field emission (TFE) for sample C (higher Ohmic) and field emission (FE) for sample D (lower Ohmic), according to the following criteria using $E_{00} = q\hbar\sqrt{N_D/m^*\varepsilon_s}/2$ ($\hbar$, the Dirac constant; m^*, the semiconductor electron effective mass; and ε_s, the semiconductor dielectric constant);[31,32] $k_B T > 2E_{00}/\ln(4\Phi_B/E_F)$ for TFE and $k_B T < 2E_{00}/[\ln(4\Phi_B/E_F) + (2E_{00}/E_F)^{1/2}]$ for FE, where k_B is the Boltzmann constant, Φ_B is the barrier height, and E_F is the semiconductor Fermi energy. In order to confirm the conduction mechanisms, we measured the temperature dependence of ρ_c obtained from the floating contact resistances. Figure 7 shows the measured ρ_c for samples C and D as a function of temperature with fitting curves. For the fitting, we employed the following models of TFE for sample C and FE for sample D[33]

$$\rho_{cTFE} = \frac{k_B^2 \cosh(E_{00}/k_B T)\sqrt{\coth(E_{00}/k_B T)}}{A^* q\sqrt{\pi(\Phi_B + E_F)E_{00}}} \times \exp\left(\frac{\Phi_B + E_F}{E_{00}\coth(E_{00}/k_B T)} - \frac{E_F}{k_B T}\right) \quad (9)$$

TABLE I. Summary of the electrical properties obtained by multi-probe Hall device measurements.

Sample		ρ_{sh} (Ω/□)	n_{s0} (10^{13} cm^{-2})	μ_{s0} (cm^2/V-s)
A: w/o metal		530	0.77	1530
Sample	ρ_c (10^{-5} Ω cm^2)	ρ_{sk} (Ω/□)	n_s (10^{13} cm^{-2})	μ_s (cm^2/V-s)
B: no Ohmic	…	540	0.73	1570
C: higher Ohmic	17 ± 1	400 ± 20	2.0 ± 0.1	800 ± 30
D: lower Ohmic	2.6 ± 0.4	330 ± 40	5.5 ± 0.7	350 ± 20

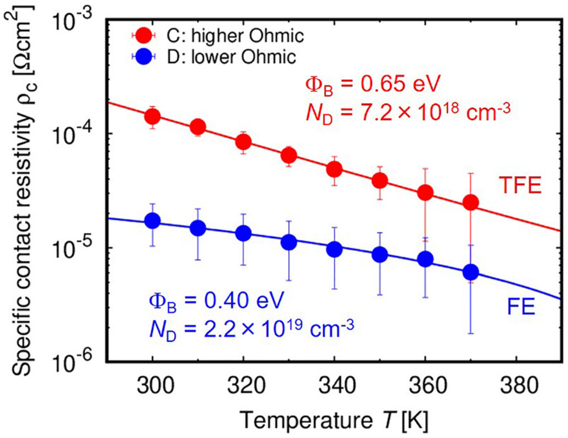

FIG. 7. The measured specific contact resistivity ρ_c for samples C and D as a function of temperature T with the fitting curves.

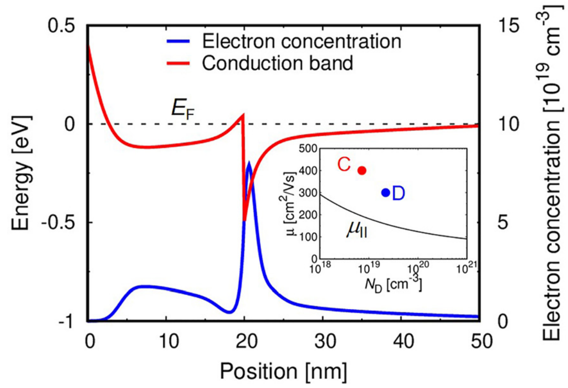

FIG. 8. The calculated band diagram of the AlGaN/GaN heterostructures under the Ohmic metal for sample D. The inset: the theoretical ionized impurity scattering mobility in AlGaN as a function of the doping concentration N_D, for the zero compensation ratio. The estimated AlGaN mobilities are given by the solid circles.

and

$$\rho_{\mathrm{cFE}} = \left[\frac{A^*\pi qT}{k_B \sin(\pi c k_B T)} \exp\left(\frac{-\Phi_B}{E_{00}}\right) - \frac{A^* q}{c k_B^2} \exp\left(\frac{-\Phi_B}{E_{00}} - cE_F\right)\right]^{-1}, \tag{10}$$

where $c = 1/2E_{00} \ln(4\Phi_B/E_F)$ and A^* is the Richardson constant. We find that the measured ρ_c is well-fitted by the TFE model for sample C, and the FE model for sample D, where the fittings give $N_D \simeq 7.2 \times 10^{18}\,\mathrm{cm}^{-3}$ and $\Phi_B \simeq 0.65$ eV for sample C, and $N_D \simeq 2.2 \times 10^{19}\,\mathrm{cm}^{-3}$ and $\Phi_B \simeq 0.40$ eV for sample D.

Based on the above N_D and Φ_B, by using the Poisson–Schrödinger calculation, we obtained the band diagram of the AlGaN/GaN heterostructures under the Ohmic metal. For the calculation, we tentatively assumed an exponentially decaying doping concentration $N_0 \exp(-z/\xi)$, which coincides the above-obtained N_D at the edge of the depletion layer, where z is the distance from the surface and ξ is the characteristic length. If we set $N_0 = 1.4 \times 10^{19}\,\mathrm{cm}^{-3}$ with $\xi = 12$ nm for sample C and $N_0 = 2.7 \times 10^{19}\,\mathrm{cm}^{-3}$ with $\xi = 20$ nm for sample D, the measurement results of the multi-probe Hall devices are well-reproduced. Figure 8 shows the band diagram for sample D, exhibiting a parallel conduction in the AlGaN and GaN layers. In general, for a system with a parallel conduction, the Hall measurement results should be[34–38]

$$n_s = \frac{\left(\sum_k \frac{n_k \mu_k}{1+\mu_k^2 B^2}\right)^2 + \left(\sum_k \frac{n_k \mu_k^2 B}{1+\mu_k^2 B^2}\right)^2}{\sum_k \frac{n_k \mu_k^2}{1+\mu_k^2 B^2}} \simeq \frac{\left(\sum_k n_k \mu_k\right)^2}{\sum_k n_k \mu_k^2} \quad \text{and} \quad \mu_s = \frac{\sum_k n_k \mu_k}{n_s} \simeq \frac{\sum_k n_k \mu_k^2}{\sum_k n_k \mu_k}, \tag{11}$$

where k represents a parallel conduction channel index, and the approximation is valid for the low-magnetic-field limit. Owing to the measurements using $B = 0.32$ T, we can utilize the low-magnetic-field approximation, while the magnetic field and temperature dependent measurements are useful to investigate the parallel conduction.[37] Using the mobility in the GaN layer of $\sim$850 cm^2/V-s for sample C and $\sim$450 cm^2/V-s for sample D, the extrapolated 2DEG mobility based on the curve in Fig. 6, the electron mobility in the AlGaN layer is estimated to be $\sim$400 cm^2/V-s for sample C and $\sim$300 cm^2/V-s for sample D.

There are several possible origins of the doping in the AlGaN layer after Ohmic contact formation, such as donor doping by nitrogen vacancies[16] or diffused metal atoms,[17] and also polarization doping[39] induced by a strain due to the Ohmic metal. For the donor doping, the dominant scattering mechanisms are ionized impurity (II) scattering[40] and bulk alloy scattering.[41] The inset of Fig. 8 shows the theoretical II scattering mobility in the AlGaN as a function of N_D for the zero compensation ratio $\theta = N_A/N_D$ (N_A, the acceptor concentration),[40] in comparison with the above-obtained AlGaN mobility. Even in the case of zero compensation ratio, the II scattering mobility is $<$200 cm^2/V-s at $N_D = 7.2 \times 10^{18}\,\mathrm{cm}^{-3}$ and $<$150 cm^2/V-s at $N_D = 2.2 \times 10^{19}\,\mathrm{cm}^{-3}$, which is rather low in comparison with the experimentally obtained mobility; the experimental results cannot be explained only by donor doping. On the other hand, polarization doping can give a high mobility even for high-density doping, owing to the absence of II scattering.[42,43] Therefore, it is suggested that polarization doping induced by a strain in the AlGaN layer has a contribution to the high doping concentration. In order to elucidate the origins of the doping, material analyses for characterization of the microstructure and the strain under the Ohmic metal will be useful.

In summary, by using multi-probe Hall devices, we characterized the electrical properties of the AlGaN/GaN heterostructures under the Ohmic metals. We find a decrease in the sheet resistance with a decrease in the Ohmic contact resistance, attributed to a significant increase in the sheet electron concentration due to high doping in the AlGaN layer, leading to an Ohmic contact dominated by field-emission. Moreover, it is suggested that polarization doping in the AlGaN layer has a contribution to the high doping concentration. Multi-probe Hall devices realize characterization of the sheet electron concentration and the electron mobility, as well as the sheet resistance, providing a useful method to characterize electrical properties of semiconductors under Ohmic metals.

DATA AVAILABILITY

The data that support the findings of this study are available from the corresponding author upon reasonable request.

REFERENCES

[1]H. Berger, Solid State Electron. **15**, 145 (1972).
[2]G. K. Reeves and H. B. Harrison, IEEE Electron Device Lett. **3**, 111 (1982).
[3]H. Kattelus, J. Tandon, and M.-A. Nicolet, Solid State Electron. **29**, 903 (1986).
[4]H. G. Henry, IEEE Trans. Electron Devices **36**, 1390 (1989).
[5]M. Ahmad, A. Shah, D. Sharma, N. Roy, and B. Arora, Solid State Electron. **46**, 505 (2002).
[6]Y. Sun, X. Chen, and L. F. Eastman, J. Appl. Phys. **98**, 053701 (2005).
[7]M. Hajłasz, J. J. T. M. Donkers, S. J. Sque, S. B. S. Heil, D. J. Gravesteijn, F. J. R. Rietveld, and J. Schmitz, Appl. Phys. Lett. **104**, 242109 (2014).
[8]M. Hajłasz, J. J. T. M. Donkers, S. J. Sque, S. B. S. Heil, D. J. Gravesteijn, F. J. R. Rietveld, and J. Schmitz, in *Proceedings of the International Conference on Microelectronic Test Structures* (IEEE, 2015), pp. 158–162.
[9]M. Spera, C. Miccoli, R. L. Nigro, C. Bongiorno, D. Corso, S. D. Franco, F. Iucolano, F. Roccaforte, and G. Greco, Mater. Sci. Semicond. Process. **78**, 111 (2018).
[10]S. Venica, F. Driussi, A. Gahoi, P. Palestri, M. C. Lemme, and L. Selmi, IEEE Trans. Electron Devices **65**, 1589 (2018).
[11]M. König, G. Ruhl, A. Gahoi, S. Wittmann, T. Preis, J.-M. Batke, I. Costina, and M. C. Lemme, IEEE J. Electron Devices Soc. **7**, 219 (2019).
[12]L. Floyd, T. Scheuermann, P. Herbert, and W. Kelly, Solid State Electron. **37**, 1579 (1994).
[13]D. Sawdai, D. Pavlidis, and D. Cui, IEEE Trans. Electron Devices **46**, 1302 (1999).
[14]M. Lijadi, F. Pardo, N. Bardou, and J.-L. Pelouard, Solid State Electron. **49**, 1655 (2005).
[15]G. Greco, F. Iucolano, and F. Roccaforte, Appl. Surf. Sci. **383**, 324 (2016).
[16]S. Ruvimov, Z. Liliental-Weber, J. Washburn, D. Qiao, S. S. Lau, and P. K. Chu, Appl. Phys. Lett. **73**, 2582 (1998).
[17]L. Wang, F. M. Mohammed, and I. Adesida, J. Appl. Phys. **101**, 013702 (2007).
[18]D. H. Zadeh, S. Tanabe, N. Watanabe, and H. Matsuzaki, Jpn. J. Appl. Phys., Part 1 **55**, 05FH06 (2016).
[19]D. Qiao, L. Jia, L. S. Yu, P. M. Asbeck, S. S. Lau, S.-H. Lim, Z. Liliental-Weber, T. E. Haynes, and J. B. Barner, J. Appl. Phys. **89**, 5543 (2001).
[20]A. Malmros, H. Blanck, and N. Rorsman, Semicond. Sci. Technol. **26**, 075006 (2011).
[21]H. Tokuda, T. Kojima, and M. Kuzuhara, Appl. Phys. Lett. **101**, 082111 (2012).
[22]H. Tokuda, T. Kojima, and M. Kuzuhara, Appl. Phys. Lett. **101**, 262104 (2012).
[23]H. Tokuda, T. Kojima, and M. Kuzuhara, Appl. Phys. Express **7**, 041001 (2014).
[24]M. Kuzuhara and H. Tokuda, IEEE Trans. Electron Devices **62**, 405 (2015).
[25]M. J. Moelter, J. Evans, G. Elliott, and M. Jackson, Am. J. Phys. Appl. **66**, 668 (1998).
[26]C. Luan, Z. Lin, Y. Lv, J. Zhao, Y. Wang, H. Chen, and Z. Wang, J. Appl. Phys. **116**, 044507 (2014).
[27]A. Gold, Phys. Rev. B **35**, 723 (1987).
[28]H. Sakaki, T. Noda, K. Hirakawa, M. Tanaka, and T. Matsusue, Appl. Phys. Lett. **51**, 1934 (1987).
[29]O. Katz, A. Horn, G. Bahir, and J. Salzman, IEEE Trans. Electron Devices **50**, 2002 (2003).
[30]L. Hsu and W. Walukiewicz, Phys. Rev. B **56**, 1520 (1997).
[31]E. L. Murphy and R. H. Good, Phys. Rev. **102**, 1464 (1956).
[32]F. Padovani and R. Stratton, Solid State Electron. **9**, 695 (1966).
[33]A. Yu, Solid State Electron. **13**, 239 (1970).
[34]R. L. Petritz, Phys. Rev. **110**, 1254 (1958).
[35]G. Ghibaudo and G. Kamarinos, Rev. Phys. Appl. **17**, 133 (1982).
[36]G. Ghibaudo, J. Phys. C **19**, 767 (1986).
[37]S. Lisesivdin, N. Balkan, and E. Ozbay, Microelectron. J. **40**, 413 (2009).
[38]M. A. Negara, D. Veksler, J. Huang, G. Ghibaudo, P. K. Hurley, G. Bersuker, N. Goel, and P. Kirsch, Appl. Phys. Lett. **99**, 232101 (2011).
[39]D. Jena, S. Heikman, D. Green, D. Buttari, R. Coffie, H. Xing, S. Keller, S. DenBaars, J. S. Speck, U. K. Mishra, and I. Smorchkova, Appl. Phys. Lett. **81**, 4395 (2002).
[40]I. Halidou, Z. Benzarti, Z. Chine, T. Boufaden, and B. E. Jani, Microelectron. J. **32**, 137 (2001).
[41]S. Bajaj, T.-H. Hung, F. Akyol, D. Nath, and S. Rajan, Appl. Phys. Lett. **105**, 263503 (2014).
[42]S. Rajan, S. P. DenBaars, U. K. Mishra, H. G. Xing, and D. Jena, Appl. Phys. Lett. **88**, 042103 (2006).
[43]M. Zhu, M. Qi, K. Nomoto, Z. Hu, B. Song, M. Pan, X. Gao, D. Jena, and H. G. Xing, Appl. Phys. Lett **110**, 182102 (2017).